**SI Appendix for:**
**Early, intensive marine resource exploitation by humans in the Middle Stone Age at Ysterfontein 1, South Africa**

Elizabeth M. Niespolo[1,2*], Warren D. Sharp[2], Graham Avery[3,4], Todd E. Dawson[5],

[1] Department of Earth & Planetary Science, University of California-Berkeley, U.S.A.
[2]Berkeley Geochronology Center, Berkeley, U.S.A.
*current address: Division of Geological and Planetary Sciences, California Institute of Technology, Pasadena, U.S.A., niespolo@caltech.edu
[3]Iziko Museums of South Africa, Cape Town
[4] Department of Archaeology, University of Cape Town, Cape Town, South Africa
[5] Department of Integrative Biology, University of California-Berkeley, U.S.A

## 1. Supplementary Background

*Samples*

Twelve kg of eggshell fragments were interspersed throughout the sequence at Ysterfontein 1 (YFT1) and are estimated to represent the equivalent material for ~58 whole eggs (1). Like many sites in South Africa, the depositional environment is ideal for preserving carbonates like ostrich eggshells, due to local substrate composition, the semi-arid to arid climate, and abundant marine biocarbonate shells buffering against calcite dissolution in the midden. We selected fragments sufficiently large (~2 × 2 cm) to minimize the possibility of vertical mixing, and those that had pristine appearances (uniform color, no spalling or fracturing). Figures S1 though S5 provide images of the dated samples. Human teeth recovered from Layer Groups 4, 5, and 13, along with selected lithic artifacts, can be found in Fig. S6.

## 2. Supplementary Methods

### 2.1 Laser Ablation and $^{230}$Th/U measurements

Samples were assigned Berkeley Geochronology Center (BGC) lab numbers (SI Dataset S1). For laser ablation analyses, each OES fragment was cut to expose the cross-section of the eggshell on a fresh surface and mounted in epoxy and polished to 3 μm grit (Figs. S1-S5). *In situ* concentrations of $^{238}$U and $^{232}$Th in eggshell samples were evaluated via laser ablation (LA) inductively coupled plasma mass spectrometry (ICP-MS) using a Photon Machines Analyte II excimer laser attached to a Thermo-Fisher NEPTUNE *Plus* ICP-MS. Analyses were normalized to Ca by monitoring $^{43}$Ca and assuming stoichiometric abundance of Ca. Magnetic field calibrations and signal intensities of $^{238}$U and $^{232}$Th were monitored using NIST 612 (37.38 and 37.79 ppm of U and Th, respectively; National Institute of Standards and Technology, 2012). Grand Canyon Travertine LC 190.3, a homogeneous calcite containing 2.52 ppm U (3), was used as an internal calcite standard and for calculating [U] of eggshells. $^{232}$Th/U ratios were corrected for the reduced sensitivity to $^{232}$Th in the plasma and ion optics via a relative sensitivity factor determined from contemporaneous analyses of ~0.1 mg carbonate samples that were dissolved, equilibrated with mixed U-Th tracer, desolvated, and analyzed. OES lines were first treated with a pre-ablation step to remove any surface contamination at 10% laser output, 0.68 J/cm$^2$ fluence,

5 Hz rep rate, 65μm spot size, and 50 μm/s scan speed. The following ablation step used 50% laser output, 3.4 J/cm$^3$ fluence, 5 Hz rep rate, 65 μm spot size, 5 μm/s scan speed, all at 4.5 mJ laser energy set point. $^{238}$U, $^{232}$Th and $^{43}$Ca were measured sequentially using magnetic field switching in cycles lasting ~7 seconds. $^{238}$U and $^{232}$Th were measured using an ion counter while $^{43}$Ca was measured on a Faraday detector.

Sub-samples from palisade layer crystals of eggshells were carefully prepared for analysis. Preparation requires systematic abrasion with a Dremel hand tool and close monitoring of the remaining sample thickness using a digital caliper to determine the position of a sub-sample relative to the outer surface. At least two spatially distinct sub-samples are necessary to apply internal reliability criteria. Weathered edges are removed by abrasion, as weathered edges may host additional U and Th taken up at a later stage from chemical weathering and/or entrainment of detritus (4), and to avoid edge effects that would violate the boundary conditions for 1-D diffusion. Large pores (single to branching angusticanuliculate pore canal morphotype, e.g., (5, 6) used by incubating chicks for breathing) are also removed by hand with a Dremel and dental burr. Macroscopic groupings of pore canals have been imaged with transmitted light and scanning electron microscopy (4, 5, 7) and with computed tomography 3-dimensional image stacks (8).

Sub-samples were dated in BGC's U-Daughter Lab via solution analyses using a Thermo-Fisher NEPTUNE *Plus* multi-collector ICP-MS. Eggshell tablets were totally dissolved in 7N $HNO_3$ and equilibrated with a mixed spike containing $^{229}$Th, $^{233}$U, and $^{236}$U. The spike was calibrated using New Brunswick National Lab CRM145 uranium solution and solutions prepared from a 69 Ma U ore from Schwartzwalder Mine, Colorado, USA that have been demonstrated to yield concordant U-Pb ages (9) and sample-to-sample agreement of $^{234}$U/$^{238}$U and $^{230}$Th/$^{238}$U ratios. U and Th were separated from sample matrix using two stages of $HNO_3$–HCl cation exchange chemistry followed by reaction with $HNO_3$ and $HClO_4$ to remove any residual organic material.

All concentration and isotopic measurements were carried out at the BGC on the NEPTUNE *Plus* ICP-MS. Samples were introduced into the ICP-MS using an Aridus II desolvator after mixing with dilute $HNO_3$-HF run solution. Each analysis included a wash step followed by an instrumental blank, the sample measurement, and a measurement of peak tails. Sample measurements were carried out in peak-jumping mode with all masses measured on Faraday collectors during multi-collection except $^{230}$Th which was measured with an ion counter. Simultaneous collection of U and Th isotopes during respective runs included measurement of $^{238}$U to normalize fluctuations in signal intensity. Instrumental backgrounds, Faraday collector baselines, and ion counter dark noise were measured at each U and Th mass while aspirating the same $HNO_3$-HF run solution used to dilute samples. Sample measurements incorporated within-run mass bias corrections using the known $^{233}$U/$^{236}$U ratio of the spike. Ion counter yield (relative to Faraday collectors) was determined during each sample measurement by cycling $^{229}$Th and $^{233}$U between the ion counter and the L1 Faraday collector. Peak tails were measured on the ion counter at seven half-mass positions from m/e = 229.5 to 241.5 while aspirating sample solution and the sum of tails from all peaks was modeled and subtracted at each U and Th mass position. Measured peak heights were corrected for Faraday baselines/ion counter dark noise, instrumental backgrounds, Faraday gains, ion counter yields, mass fractionation, peak-tails, procedural blanks, and interfering spike isotopes. The external reproducibility of $^{234}$U/$^{238}$U and $^{230}$Th/$^{238}$U ratios of Schwartzwalder Mine (SCH) solutions measured during analytical sessions was better than 0.2% and 0.4%, respectively. Unknowns were normalized to SCH reference values measured in the

same run sequence to correct for run-to-run bias. Procedural blanks for $^{238}U$, $^{232}Th$, and $^{230}Th$ ranged, in pg, from 189.2 to 376.2, from 0.006 to 3.7, and 0.000027 to 0.000033, respectively, and were subtracted from samples. Activity ratios and ages were calculated using the half-lives of Jaffey et al. (1971) for $^{238}U$, Holden (1990) for $^{232}Th$, and Cheng et al. (2013) for $^{230}Th$ and $^{234}U$. Initial ($^{234}U/^{238}U$) is back calculated from measured ($^{234}U/^{238}U$) and the corrected $^{230}Th/U$ age.

The $^{232}Th$ contents of OES samples were used to correct for unsupported $^{230}Th$ (i.e., $^{230}Th$ not produced by *in situ* decay of secondary U). $^{232}Th$ is not a product of U decay and its presence that associated $^{230}Th$ is present. $^{232}Th$ has a half-life of $1.405 \times 10^{10}$ a and can be treated as a stable isotope on Quaternary timescales (the timescales at which $^{230}Th/U$ dating is applicable). $^{232}Th$ thus serves as an index for the amount of extraneous $^{230}Th$ incorporated into the eggshells. By measuring the amount of $^{232}Th$ in a sample and assuming a $^{230}Th/^{232}Th$ ratio for the unsupported $^{230}Th$, typically that of upper crustal silicates, extraneous $^{230}Th$ may be estimated and subtracted from the sample (e.g., (13). To make such a correction for OES, we assume the unsupported $^{230}Th$ comes from fine-grained detritus derived from host sediments, which is often visibly present, and that the detritus is at or near secular equilibrium and has a crustal Th/U ratio. Specifically, we assign the following values and uncertainties to the detritus: ($^{232}Th/^{238}U$) = 1.21 ± 0.5; ($^{230}Th/^{238}U$) = 1 ± 0.1; ($^{234}U/^{238}U$) = 1 ± 0.1, subtract the indicated U and Th from samples, and propagate resulting uncertainties into the final age-errors. Ages and uncertainties were calculated using Isoplot 3.75 and do not include uncertainties in decay constants (14). Samples from layer group 1 were analyzed on December 20, 2017; from layer group 12 on March 15, 2018; and from layer groups 3, 6, and 10 on July 26, 2018. Data is reported using guidelines from (15). All activity ratios are provided in SI Dataset S1B.

### 2.2 Stable Isotopes

OES fragments were mechanically abraded on all surfaces with a Dremel hand drill and then cleaned by sonication in Millipore water. Samples are dried and weighed, and then 20-30 wt.% of the sample is leached in 1N HCl. The remaining sample is rinsed in Millipore water and dried. A ~sub-mg-sized sample is drilled out in cross section of the leached OES fragment for isotopic analysis of the calcite fraction, ensuring that the sampled calcite represented a homogenized sample of the eggshell after leaching, primarily derived from the palisade layer crystals. The organic fraction, mainly proteins and polysaccharides (hereafter referred to as the total organic fraction or TOF), was purified by leaching the remaining carbonate fraction of the eggshell in 1N HCl. After complete dissolution of the calcite fraction, the TOF is rinsed and centrifuged repeatedly to reduce the pH to near-neutral levels and then freeze-dried. The TOF is then weighed and packed in tin capsules for mass spectrometric analysis.

Stable isotope abundances are reported in delta (δ) notation in parts per thousand (‰) where: $\delta = ((R_A/R_S) - 1) \times 1000$, and $R_A$ and $R_S$ are the ratios of the rare to abundant isotope ($^{18}O/^{16}O$, $^{15}N/^{14}N$, or $^{13}C/^{12}C$) in the sample of interest and in an international standard, respectively. Isotopic analyses were completed in the UC Berkeley Center for Stable Isotope Biogeochemistry (CA, U.S.A.). $\delta^{13}C$ and $\delta^{18}O$ values of the extracted calcite fraction of OES were analyzed using an IsoPrime-DI-MultiPrep system to dissolve samples in $H_3PO_4$ at 90° C, in line with a GV IsoPrime mass spectrometer in dual inlet mode. Three internal laboratory standards and an international standard were used for calibration and/or quality control. These laboratory reference materials are calibrated annually against IAEA (International Atomic

Energy Agency, Vienna, Austria) certified reference materials. Calcite $\delta^{13}C$ values are calibrated relative to international standard NBS 19 (limestone) and reported relative to the international standard Vienna Pee Dee Belemnite (VPDB; Hut, 1987). Calcite $\delta^{18}O$ values are reported according to Vienna Standard Mean Ocean Water (VSMOW; Coplen, 1996). Run precision based on within-run reproducibility of the quality control standard were 0.084‰ and 0.055‰ for $\delta^{13}C$ and $\delta^{18}O$ values, respectively, for selected samples in italics (SI Dataset S1D; all errors 1σ), and 0.092‰ and 0.079‰ respectively for non-italicized samples. Long-term precisions of $\delta^{13}C$ and $\delta^{18}O$ values are respectively 0.05‰ and 0.07‰.

The TOF of OES was analyzed using a CHNOS Elemental Analyzer interfaced to an IsoPrime 100 mass spectrometer. Raw data were calibrated using standards NIST (National Institute of Standards and Technology, Gaithersburg, MD, USA) Standard Reference Material (SRM) 1577b (bovine liver) and SRM 1547 (peach). The international standards (relative to which the TOF delta values are reported) are atmospheric nitrogen (air) for $\delta^{15}N$ values and VPDB for $\delta^{13}C$ values. Raw instrument data were corrected for drift over time and linearity and normalized to the international stable isotope reference scale. Run precision is ±0.1‰ and ±0.2‰ for $\delta^{13}C$ and $\delta^{15}N$, respectively, except where specified otherwise in the SI Dataset S1D. Long-term external precision is ± 0.10‰ and ± 0.15‰, respectively for C and N isotope analyses. For both calcite and TOF analyses, standards were added throughout the run for raw data corrections and to measure accuracy and precision. Modern OES fragments deriving from the same egg were prepared in the same way as the ancient OES, and analyzed with each batch of TOF analyses, as a procedural standard under development. Prior results yielded $\delta^{15}N = 7.0 \pm 0.5$‰ and $\delta^{13}C = -24.0 \pm 0.4$‰ for the modern egg (18). The modern procedural samples prepared with YFT1 samples were all within uncertainty of prior-reported results for the modern eggshell, with $\delta^{15}N$ values ranging from 6.9 to 7.1‰ and $\delta^{13}C$ from -24.2 to -24.3‰. Statistical analyses on data sets were performed in R (19).

Equations used to calculate proxy delta values ($\delta^{13}C_{diet}$ and $\delta^{18}O_{foliarH2O}$) and mean annual precipitation are based on modern empirical calibrations and understanding the ecological and climatological factors contributing to each isotope system in ostrich eggshells. A brief explanation and relevant equations are provided here. Detailed explanations for these can be found in (20) and (18).

Wild ostriches are opportunistic water-conserving herbivores that feed almost entirely on green plants within their home range with a slight dietary preference for $C_3$ plants (e.g., leafy plants better adapted to cooler and/or wetter climates), but they generally sample the ambient vegetation in correspondence with the abundance of available plant groups (21, 22). Hence, the $\delta^{13}C$ values of their tissues is related to their diet and generally to the ambient vegetation in their home range area (~85 $km^2$ daily). The dietary $\delta^{13}C$ values are related to both the calcite and total organic fraction (TOF) of ostrich eggshells:

$$\Delta^{13}C_{calcite\text{-}diet} = \delta^{13}C_{calcite} - \delta^{13}C_{diet} = +16.2 \pm 0.5‰$$

and

$$\Delta^{13}C_{TOF\text{-}diet} = \delta^{13}C_{TOF} - \delta^{13}C_{diet} = +1.5 \pm 0.8‰.$$

In modern OES, the difference between the $\delta^{13}C$ values of eggshell calcite and TOF reflect a constant biological fractionation $\Delta^{13}C_{calcite\text{-}TOF} = 14.7‰$ (20). This $\Delta^{13}C_{calcite\text{-}TOF}$ relation

should also apply in well-preserved ancient eggshells and is a necessary condition for inferring that primary C and N isotope values have been retained by ancient OES. Accordingly, (20) recommended a widely accepted criterion of $\Delta^{13}C_{calcite\text{-}TOF} = 15 \pm 2‰$ and we employ this as a screening tool to qualify samples with pristine TOF (Fig. S8).

While two models were proposed by Niespolo et al. (ref. 18) to estimate $\delta^{18}O_{foliarH2O,}$ both utilize the fractionation factor ($\alpha$) between ostrich body water and eggshell calcite ($\alpha_{calcite\text{-}bodyH2O} = 1.0379 \pm 0.002$; Passey et al., 2014) to back-calculate $\delta^{18}O_{bodyH2O}$ values. We employ the model from (18) that keeps the calculated $\delta^{18}O_{foliarH2O}$ values independent from the other isotope systems (namely, $\delta^{13}C$ values). This approach adapts a model by (24) relating body waters to the source dietary waters for a variety of eastern African herbivores (for ostriches, as non-obligate drinkers, this is foliar water); for birds, the relationship is modeled by the equation

$$\delta^{18}O_{bodyH2O} = 5.83‰ + 0.71 * \delta^{18}O_{foliarH2O}$$

$\delta^{18}O_{foliarH2O}$ values change with changes in evapotranspiration which is environmentally modulated by temperature and relative humidity (25). Increasing $\delta^{18}O_{foliarH2O}$ values correspond with increasing temperature and/or decreasing relative humidity (RH). Thus, $\delta^{18}O_{foliarH2O}$ values modelled from the $\delta^{18}O_{OES}$ provide a record of changes in temperature and relative humidity. $\delta^{18}O_{OES}$ co-vary with $\delta^{18}O_{foliarH2O}$; thus, increasing $\delta^{18}O_{OES}$ also correspond with increasing temperature, and/or decreasing RH.

We can estimate paleo-mean annual precipitation (paleo-MAP) using the inverse relationship in ref. 18):

$$\delta^{15}N = -0.01 \times (PMAP) + 14.59‰$$

From the $\delta^{13}C_{diet}$ values, we calculate the fraction of $C_4$ plants in the diet f($C_4$) using mean values of -27‰ and -11.5‰ for $C_3$ and $C_4$ plants, respectively, which are 1.5‰ lower than recommended modern average values for each photosynthetic pathway (26, 27). This is to account for a ~1.5‰ decrease in the average $\delta^{13}C$ of atmospheric $CO_2$ from post-industrial plants sampled by these modern studies due to the Suess Effect (e.g., 28–30).

## 3. Supplementary Results & Discussion

### 3.1 Distribution of U and U isotopes in ostrich eggshells

Uptake of secondary U in OES is controlled by primary eggshell structures and common Th ($^{232}Th$) varies systematically with distance from inner and outer eggshell surfaces (4, 31, 32). In the OES from YFT1, steep smooth gradients of U and Th begin at the outer surface in the vertical crystal layer, the outer ~50um of the eggshell. [U] concentrations are flattest and vary the least in the radially oriented columnar calcite crystals internal to eggshell surfaces called “palisade” crystals. Near-zero [U] occurs as the palisade crystals transition to cone crystals, comprising the inner ~25% of the eggshell. These primary values occur where nano-scale porosity is lowest, followed by highly nano-porous cone and mammillary knob structures (7) where erratic U concentrations occur. (Figure 2, main text; Figs. S1-S5). The shallow slope of [U] across the palisade layer crystals indicates fast diffusion of U (Fig. S7) (32); this indicates

rapid U uptake across the palisade layer crystals. Changes in the U concentration correspond to changes in crystal habit and micropore density, suggesting that U transport is mediated by eggshell structure.

OES from the same layer groups have similar [U] in their palisade layer crystals (Fig. S9). Samples higher in the YFT1 sequence have higher [U] than samples deep in the section and mean [U] in palisade layer crystals similarly decreases with decreasing stratigraphic depth (main text Figure 2). Permeability may decrease with increasing depth if sediment accumulation causes compression. Sediments at YFT1 are made of calcareous sands hosting heterogeneously scattered cobbles of calcrete, aeolianite, and diorite (the host rock lithology of the shelter; (1, 36), which may have spatially heterogeneous permeability and compositions of soil leachates. A thick calcrete divides the upper Layer Groups 1-6 from lower Layer Groups 7-13 which may act as an aquitard. Below Layer Group 6, sediments with varying and patchy carbonate cementation seal the matrix in clast-supported, entirely human-accumulated shell midden layers. It is possible that paleoclimatic effects like effective moisture may affect U uptake, but this is likely to be more relevant to sites in more extreme precipitation regimes, such xeric climates, where little to no water might move through sediments for prolonged intervals. Since YFT1 is situated in a temperate climate with a consistent winter rainy season at the coast, and the sediments are dominated by carbonate-sands, it is likely that moisture levels in host sediments were sufficient to promote U uptake upon burial, consistent with the observed stratigraphic coherence of 10 out of 11 the $^{230}$Th/U ages.

While 10 of 11 samples with reliable burial ages have calculated $(^{234}U/^{238}U)_0$ in agreement between tablets, one such sample (YFT1-10E) has distinct $(^{234}U/^{238}U)_0$ between the outer and inner shell samples, suggesting there may have been a change in the pore water U isotopic composition during U uptake in this sample. This may occur from changes in pore water trace element composition, changes to the extent of the vadose zone, or permeability near the OES fragment.

$(^{234}U/^{238}U)_0$ ratios agree among some OES fragments in the same Layer Group (e.g., samples in Layer Groups 1 and 6) and some Layer Groups have groups of samples with distinctive $(^{234}U/^{238}U)_0$ (e.g., samples in layer groups 10 and 12; Fig. S9). While $(^{234}U/^{238}U)$ ratios can be homogeneous within a single Layer Group (as demonstrated by similar $(^{234}U/^{238}U)$ between samples in Layer Groups 1 and 6), heterogeneity in layer groups 10 and 12 implies that soil pore water $(^{234}U/^{238}U)$ can vary at sub-meter spatial scales and there may be fine scale heterogeneity of pore water $(^{234}U/^{238}U)$ within a similar matrix. This is consistent with studies of pedogenic carbonates where carbonates that precipitated on different clasts in the same time interval and soil profile yielded distinct $(^{234}U/^{238}U)_0$ (33). This is perhaps not surprising since the YFT1 sediments are mineralogically heterogeneous, and spatial variations in minerology, even at the sub-meter scale, may affect local [U] and $(^{234}U/^{238}U)$ ratios in pore waters and therefore in OES. Hence, $(^{234}U/^{238}U)_0$ in OES should serve as a proxy for soil pore water $(^{234}U/^{238}U)$ at the time of uptake. Soil pore water $(^{234}U/^{238}U)$ has been proposed as quantitative paleohydrologic indicator in pedogenic, speleothem, and lacustrine carbonates, since it is expected to vary with infiltration rates (34). $(^{234}U/^{238}U)_0$ in OES thus could provide an additional paleohydrologic proxy. With larger data sets, these may be integrated into paleoclimate models to elucidate past infiltration and precipitation, as has been done with more traditionally collected pedogenic carbonate clast-coatings (34, 35).

### 3.2 $^{230}$Th/U Geochronology

Ostrich eggshells (OES) are ~2-mm thick, composed of ~97-99% low-Mg calcite with 1-3% organics, and they are geochemically suitable for U-series (or $^{230}$Th/U) dating. Although most uranium in ostrich eggshell is acquired after burial, accurate depositional ages can be determined when two or more subsamples of each OES are dated and the measured $^{230}$Th/U ages are corrected using a simple diffusion model; such ages are termed "$^{230}$Th/U burial ages" (4). $^{230}$Th/U burial ages mark the time when the OES fragment was buried along with other associated archaeological materials, assuming U uptake begins upon burial as discussed above. Prior method development of $^{230}$Th/U burial dating emphasized comparison of $^{230}$Th/U ages with $^{14}$C dates on the same OES and demonstrated that criteria inherent to the $^{230}$Th/U data could be used to assess the fidelity of $^{230}$Th/U burial ages (4). Ages by two independent methods (one which dates the time of eggshell mineralization, and the other which dates the time of burial) were indistinguishable within uncertainties for most eggshells (4), implying that correction using a simple diffusion model yielded improved $^{230}$Th/U ages. Because Ysterfontein 1 is known to be older than the ~45 ka limit of $^{14}$C dating, in addition to the use of these geochemical criteria, we utilize stratigraphic principles and other known geological and chronological constraints to evaluate the new $^{230}$Th/U ages. Our results relative to previous dating work (1, 36) provide a much more precise and accurate constraint on the occupation of YFT1.

There are a number of geochemical processes that could modulate the uptake of trace elements in biominerals (37–40), including diffusion-limited processes, if the structure of the concentration profile can be simplified to 1 dimension (1-D). For 1-D diffusion, the time it takes for a substrate to diffuse a certain distance from the diffusion surface is related to the square of that distance. If U is taken up and fixed at a distance from the diffusion surface, U-series ages in OES should decrease with distance-squared from the diffusion surface, and the age at the diffusion surface would represent the time that U was first taken up upon burial. Kohn (ref. 37) showed that by normalizing these variables, the uptake of trace elements into fossil materials could be modelled by diffusion from a single surface.

U concentration profiles and profile structure in the radial direction is consistent with a 1-D diffusion model starting from the outer surface of the eggshell. This is also apparent from the small means and uncertainties on 5 lines of laser ablation measurements from a single eggshell (Fig. S7; SI Dataset S1C), making 1-D uptake from the outer to inner surface a reasonable model to characterize U uptake. As such, we apply a simple 1-D diffusive uptake model to determine the time when the OES fragments were first exposed to U in soil pore water. With absolute ages of sub-samples at different distances from the diffusion surface from U-series measurements, we plot the relationship between these ages and the normalized-distance-squared of sub-samples from the diffusion surface. By plotting ages of sub-samples relative to the normalized distance-squared from the outer surface, where trace element uptake begins, the relationship becomes mathematically linear between age and distance into the sample from the surface where U uptake begins (4, 37). Linear extrapolation to the outer surface, where U would be taken up first upon burial, is defined as the $^{230}$Th/U burial age of the sample. Figures S1 through S5 provide sample images, laser ablation data, and burial age diagrams for 17 OES samples.

### 3.3 Stable Isotopes

Ostriches are broadly unselective feeders, and the carbon, nitrogen, and oxygen isotopic compositions of ostrich eggshells record the local environment on a seasonal timescale (22). This is because 1) the home range of daily food sources of ostriches is ~85 $km^2$ (21, 22); 2) eggshells mineralize rapidly and their isotopic composition reflects the diet immediately prior to the egg-laying season (20, 41, 42); and 3) the foraging habits of humans imply they are likely to sample more than one clutch (or nest) of eggs (43). To elaborate on these points, eggshells rapidly form in <24 h and their stable isotope composition reflects a "snapshot" of the ostrich diet of the prior ~3-5 days (20). Ostriches lay eggs annually over a period of ~2 weeks after the rainy season (44–46). Thus, there are a number of reasons why sampling many eggshells is important, and why the isotope data may have more variation than can be fit by a Gaussian distribution. For example, variations in eggshells laid in a single rainy season by different females could be attributed to variation in foraging and/or nesting areas proximal to human occupation sites, where humans may be most likely to forage for eggs. It may also be due to sampling eggs from different years in an archaeological horizon representing many years. Miller and Fogel (2016) (ref. 47) showed in a random sampling of 126 Holocene eggshell fragments of *Dromaius novaehollandie* (emu) from an aeolian deflation deposit, deriving from an arid climate with variable inter-annual rainfall, $\delta^{18}O$ values converged on a mean with a standard deviation of ~1-2‰ after ~20 samples. Larger suites of ostrich eggshell from the more recent past could be utilized for a similar exercise in future work. However, there are currently no robust ways to determine if two eggs are from different shells, aside from having different stable isotope compositions, so it is possible the convergence on a smaller standard deviation may derive from sampling multiple fragments from the same egg, if such samples derive from stratified archaeological excavations where one might expect to find multiple fragments from a single egg. For the YFT1 sample, in an effort to smooth out variation introduced by feeding habits of individual birds, and interannual variations in vegetation and rainfall, we evaluate multiple OES per time interval, and we take the simple mean and standard deviation as a measure of the average value from each horizon for a minimum of five samples. If a minimum of five samples is not available per layer, we pool data from multiple layers to achieve a larger sample size contributing to the average value. This data set is the largest of its kind for a South African site.

Fig. S10 shows little overlap between multiple fragments in isotope biplots, making it unlikely that individual fragments represent repeated sub-sampling of the same whole egg. Correlation between C, N, and O isotopes were generally not significant (Fig. S10, Table S1). This implies the isotope systems aren't co-varying systematically and thus paleo-environmental variables controlling one system may not be significantly impacting the other systems.

We assessed trends in mean stable isotope values for each Layer Group and have run t-tests to compare the data from adjacent layers. T-tests, conducted in R (19), take the mean of a data set and compare it to another, factoring in the distribution of each data set, and the t-test determines if the means are likely to represent statistically distinct populations of data. We have run both Welch's t-tests (assumes equal variance between the two data sets) and simple t-tests (no assumption of equal variance) for data sets of adjacent Layer Groups. All of these results are provided in SI Dataset S1F. Given there are different numbers of samples in each Layer Group (each data set), most of the Layer Groups have fewer than 10 data points to evaluate, and we cannot be certain that each data set captures the same amount of time, we prefer the simple t-tests in which there is no assumption of equal variance. The results from these tests indicate that there

are significant differences in mean values between various layers for two LG comparisons of mean $\delta^{13}C$ values, for three LG comparisons of mean $\delta^{18}O$ values, and for two LG comparisons of mean $\delta^{15}N$ values (for $p < 0.1$). The mean $\delta^{13}C$ values between LG 2 and LG 3, between LG 3 and LG 4, between LG 4 and LG 6, and between LG 6 and LG 8/9, are also significantly different based on this p-value criterion. Mean $\delta^{18}O$ values between LG 4 and LG 6, between LG 6 and LG 8/9, and between LG 8/9 and LG 10 are also significantly different. While small changes are apparent in mean $\delta^{13}C$ and $\delta^{18}O$ values in intermediate layers, uni-directional trends in these systems were not apparent as demonstrated by comparison of LG 12 to LG 1. In contrast, $\delta^{15}N$ values demonstrated significant differences between mean values. The mean $\delta^{15}N$ values between LG 1/2 and LG 4, and between LG 10/11 and LG 12, are significantly different, as well as the difference from the base to the top of the shelter (LG 12 compared to LG 1/2). All changes moving up section trend in the same direction – mean $\delta^{15}N$ values become higher through the section – thus indicating a uni-directional trend of increasing values through time, correspondent with a uni-directional trend of decreasing paleo-MAP through time. The t-tests collectively support the interpretation that there are statistically significant paleoenvironmental changes, associated with changing mean delta values, occurring in the YFT1 occupation interval.

The $\delta^{13}C$ and $\delta^{18}O$ values of OES calcite were measured on all sub-samples prepared for geochronology and are provided in Table S2. Pairs are plotted in Fig. S11 and there are some trends between tablets. Differences in isotope ratios between two tablets from the same OES range from 0.13 to 1.94‰ (for $\delta^{13}C$; median = 0.97‰) and from 0.1 to 1.31‰ (for $\delta^{18}O$; median = 0.15‰), in several cases exceeding measurement uncertainties (i.e., for most samples, 0.179‰ and 0.149‰, respectively, for $\delta^{13}C$ and $\delta^{18}O$). There is no systematic relationship in the $\delta^{18}O$ values: the inner tablet is isotopically heavier than the outer tablet in some samples and it is lighter in others. This is not surprising since oxygen isotopes in biominerals are controlled by many factors. For ostriches, factors such as the amount of atmospheric oxygen incorporated varying with respiration and thermoregulation, the isotopic composition of consumed waters (namely foliar water), and water lost during excretion or evaporation mainly impact the $\delta^{18}O$ values of body water. If biological functions (e.g., excretion, respiration, thermoregulation) are operating at differing degrees over the period of egg biomineralization (~24 hours or less) for different egg-laying events, then there may be changes to the reservoir for oxygen contributing to biomineral calcite leading to heterogeneous changes in the $\delta^{18}O$ values of eggshell calcite from a single egg-laying event. However, this implies that the intra-sample variation cannot be characterized or corrected for systematically, and that variation of this magnitude could erroneously portray some distinguishable difference between two samples outside of analytical uncertainty. With this knowledge, it is important to consider oxygen isotope data ($\delta^{18}O$ values) only when larger sample sizes are available, considering the statistical results of those data sets, rather than relying on individual data points or small data sets.

Unlike $\delta^{18}O$ values, the $\delta^{13}C$ values of the outer shell show a systematic relationship to the inner shell values, in that they are consistently higher than those of the inner shell. The carbon isotope system in biominerals is simpler than the oxygen isotope system, as there aren't competing effects on the variation of calcite $\delta^{13}C$ values besides diet. If the reservoir for carbon is finite during eggshell mineralization (deriving from a reservoir of $CO_2$ in the body), preferential use of light carbon in forming the early stages of the eggshell may produce an isotopic reservoir effect on the later stages of eggshell mineralization, leading to enriched $\delta^{13}C$ values in later stages of eggshell mineralization.

The biomineralization process may explain the systematic differences in $\delta^{13}C$ values, and eggshell mineralization is heavily studied for agricultural and evolutionary research, so we have a good understanding of eggshell mineralization rates and processes. Organic cores (also called mammillary knobs) aggregate to coat the albumen surfaces to provide the framework for calcite mineral nucleation; calcite growth continues around and upon organic proteinaceous hexagonal-web structures to create the mammillary cone and palisade crystal layers of the eggshell (5, 41). The outer ~50 μm-thick vertical crystal layer is mineralized last with a nanocrystalline film of hydroxyapatite covering the outer surface of the OES, possibly linked to cessation of eggshell mineralization in the avian oviduct (42, 48). A final, thin layer of organic cuticle coats the outer surface of the eggshell but is quickly degraded in geologic environments and hence it is not preserved on ancient eggshells. The mineralization process may explain the systematic differences in $\delta^{13}C$ values, because simply put, eggshell mineralization starts at the inner surface and mineralizes outward. Thus, a reservoir effect, in extreme cases referred to as a "starvation effect" in biologically mediated isotopic systems, would lead to a systematically isotopically heavier pool of carbon in the ostrich body from which the eggshell calcite is produced, as eggshells are mineralized, if enough light carbon is exhausted in this process. The systematic difference between tablets of palisade layer crystal $\delta^{13}C$ values could be explained this way. Alternatively, eggshell mineralization is the fastest known biomineralization process known on Earth, with eggs fully forming in less than 24 hours (e.g., 41, 43), and kinetic effects may also explain the systematically heavier outer tablets with respect to $\delta^{13}C$ values. In either case, the systematic offsets may cause concern for interpreting the $\delta^{13}C$ values of OES, but all other carbonate samples in the data set were sampled in cross-section through palisade layer crystals, thus homogenizing the signal from the inner and outer portions of the palisades. This would better reflect the overall carbon pool from the ostrich body compared to $\delta^{13}C$ values from sub-samples. Uncertainties in calculated proxy results, for even individual samples, obscure the systematic offsets seen in the measured $\delta^{13}C$ values of calcite (propagated uncertainty for a calculated $\delta^{13}C_{diet} = \sim 0.8‰$, $1\sigma$). In light of this, it is recommended that any sampling methods for isotope measurements of OES calcite be explicitly described in methods sections to consider the potential biases that may be imposed by inconsistent sampling approaches, or preferential sampling of one sub-section of OES.

**SI Appendix References**


1. G. Avery, *et al.*, The Ysterfontein 1 Middle Stone Age Rock Shelter and the Evolution of Coastal Foraging. *Goodwin Ser.* **10**, 66–89 (2008).
2. National Institute of Standards and Technology, Certificate of Analysis Standard Reference Material ® 612 Trace Elements in Glass. 612 (2012).
3. R. Mertz-Kraus, *et al.*, In situ $^{230}$Th–$^{232}$Th–$^{234}$U–$^{238}$U analysis of silicate glasses and carbonates using laser ablation single-collector sector-field ICP-MS. *J. Anal. At. Spectrom.* **25**, 1895 (2010).
4. W. D. Sharp, *et al.*, $^{230}$Th/U Burial Dating of Ostrich Eggshell. *Quat. Sci. Rev.* **219**, 362–276 (2019).
5. K. E. Mikhailov, Fossil and recent eggshell in amniotic vertebrates: fine structure, comparative morphology and classification. *Spec. Pap. Palaeontol.* **56**, 1–80 (1997).
6. E. G. F. Sauer, Ratite eggshells and phylogenetic questions. *Bonner Zool. Beitraege* **23**, 3–48 (1972).
7. E. M. Niespolo, *et al.*, Patterns of U uptake and implications for diagenesis and trace element records in biomineral eggshell in *American Geophysical Union*, (2019).
8. S. L. Loewy, *et al.*, Improved accuracy of U-series and radiocarbon dating of ostrich eggshell using a sample preparation method based on microstructure and geochemistry: A study from the Middle Stone Age of Northwestern Ethiopia. *Quat. Sci. Rev.* **247**, 106525 (2020).
9. K. R. Ludwig, A. R. Wallace, K. R. Simmons, The Schwartzwalder uranium deposit, II: Age of uranium mineralization and lead isotope constraints on genesis. *Econ. Geol.* **80**, 1858–1871 (1985).
10. A. H. Jaffey, K. F. Flynn, L. E. Glendenin, W. C. Bentley, A. M. Essling, Precision measurement of half-lives and specific activities of U235 and U238. *Phys. Rev. C* **4**, 1889–1906 (1971).
11. N. E. Holden, Total half-lives for selected nuclides. **62**, 941–958 (1990).
12. H. Cheng, *et al.*, Improvements in $^{230}$Th dating, $^{230}$Th and $^{234}$U half-life values, and U-Th isotopic measurements by multi-collector inductively coupled plasma mass spectrometry. *Earth Planet. Sci. Lett.* **371**–**372**, 82–91 (2013).
13. K. R. Ludwig, J. B. Paces, Uranium-series dating of pedogenic silica and carbonate, Crater Flat, Nevada. *Geochim. Cosmochim. Acta* **66**, 487–506 (2002).
14. K. R. Ludwig, "Using Isoplot/Ex, Version 3.75: A Geochronological Toolkit for Microsoft Excel" (2010).
15. A. Dutton, *et al.*, Data reporting standards for publication of U-series data for geochronology and timescale assessment in the earth sciences. *Quat. Geochronol.* **39**, 142–149 (2017).
16. G. Hut, "Consultants' group meting on stable isotope reference samples for geochemical and hydrological investigations" (1987).
17. T. B. Coplen, New guidelines for reporting stable hydrogen, carbon, and oxygen isotope-ratio data. *Geochim. Cosmochim. Acta* **60**, 3359–3360 (1996).
18. E. M. Niespolo, *et al.*, Carbon, nitrogen, and oxygen isotopes of ostrich eggshells provide site-scale Pleistocene-Holocene paleoenvironmental records for eastern African archaeological sites. *Quat. Sci. Rev.* **230**, 106142 (2020).
19. R Core Team, R: A language and environment for statistical computing (2018).
20. B. J. Johnson, M. L. Fogel, G. H. Miller, Stable isotopes in modern ostrich eggshell: A

calibration for paleoenviromental applications in semi-arid regions of southern africa. *Geochim. Cosmochim. Acta* **62**, 2451–2461 (1998).
21. J. B. Williams, *et al.*, Field Metabolism , Water Requirements , and Foraging Behavior of Wild Ostriches in the Namib. *Ecology* **74**, 390–404 (1993).
22. S. . J. Milton, R. J. Dean, W. R. Siegfried, Food Selection by Ostrich in Southern Africa. *J. Wildl. Manage.* **58**, 234–248 (1994).
23. B. H. Passey, *et al.*, Triple oxygen isotopes in biogenic and sedimentary carbonates. *Geochim. Cosmochim. Acta* **141**, 1–25 (2014).
24. M. J. Kohn, Predicting animal $\delta^{18}O$: Accounting for diet and physiological adaptation. *Geochim. Cosmochim. Acta* **60**, 4811–4829 (1996).
25. A. Kahmen, *et al.*, Cellulose $\delta^{18}O$ is an index of leaf-to-air vapor pressure difference (VPD) in tropical plants. *Proc. Natl. Acad. Sci.* **108**, 1981–1986 (2011).
26. M. J. Kohn, Carbon isotope compositions of terrestrial C3 plants as indicators of (paleo)ecology and (paleo)climate. *Proc. Natl. Acad. Sci.* **107**, 19691–19695 (2010).
27. J. R. Ehleringer, T. E. Cerling, C3 and C4 Photosynthesis. *Encycl. Glob. Environ. Chang.*, 186–190 (2002).
28. G. D. Farquhar, J. R. Ehleringer, K. T. Hubick, Discrimination and Photosynthesis. *Annu. Rev. Plant Physiol. Plant Mol. Biol.* **40**, 503–537 (1989).
29. C. D. Keeling, The Suess effect: 13Carbon-14Carbon interrelations. *Environ. Int.* **2**, 229–300 (1979).
30. R. F. Keeling, *et al.*, Atmospheric evidence for a global secular increase in carbon isotopic discrimination of land photosynthesis. *Proc. Natl. Acad. Sci.* **114**, 10361–10366 (2017).
31. W. D. Sharp, N. D. Fylstra, J. T. Faith, D. J. Peppe, C. A. Tryon, U-series dating of ostrich eggshell in *Goldschmidt*, (2014), p. 2265.
32. E. M. Niespolo, *et al.*, Patterns of Secondary U in ostrich eggshell: Applicaiton to U-Th dating of Quaternary terrestrial strata in *Geochemical Society*, (2017).
33. W. D. Sharp, K. R. Ludwig, O. A. Chadwick, R. Amundson, L. L. Glaser, Dating fluvial terraces by $^{230}Th/U$ on pedogenic carbonate, Wind River Basin, Wyoming. *Quat. Res.* **59**, 139–150 (2003).
34. K. Maher, *et al.*, Uranium isotopes in soils as a proxy for past infiltration and precipitation across the western United States. *Am. J. Sci.* **314**, 821–857 (2014).
35. E. J. Oerter, *et al.*, Pedothem carbonates reveal anomalous North American atmospheric circulation 70,000–55,000 years ago. *Proc. Natl. Acad. Sci.* **113**, 919–924 (2016).
36. R. G. Klein, *et al.*, The Ysterfontein 1 Middle Stone Age site, South Africa, and early human exploitation of coastal resources. *Proc. Natl. Acad. Sci.* **101**, 5708–5715 (2004).
37. M. J. Kohn, Models of diffusion-limited uptake of trace elements in fossils and rates of fossilization. *Geochim. Cosmochim. Acta* **72**, 3758–3770 (2008).
38. M. J. Kohn, R. J. Moses, Trace element diffusivities in bone rule out simple diffusive uptake during fossilization but explain in vivo uptake and release (2012) https:/doi.org/10.1073/pnas.1209513110.
39. S. M. Eggins, *et al.*, In situ U-series dating by laser-ablation multi-collector ICPMS: New prospects for Quaternary geochronology. *Quat. Sci. Rev.* **24**, 2523–2538 (2005).
40. A. W. G. Pike, R. E. M. Hedges, P. Van Calsteren, U-series dating of bone using the diffusion-adsorption model. *Geochim. Cosmochim. Acta* **66**, 4273–4286 (2002).
41. Y. Nys, M. T. Hincke, J. L. Arias, J. M. Garcia-Ruiz, S. E. Solomon, Avian eggshell mineralization. *Poult. Avian Biol. Rev.* **10**, 143–166 (1999).

42. Y. Nys, J. Gautron, J. M. Garcia-Ruiz, M. T. Hincke, Avian eggshell mineralization: Biochemical and functional characterization of matrix proteins. *Comptes Rendus - Palevol* **3**, 549–562 (2004).
43. R. L. Kelly, *The Lifeways of Hunter-Gatherers: The Foraging Spectrum* (Cambridge University Press, 2013).
44. W. Leuthold, Notes on the Breeding Biology of the Ostrich *Struthio Camelus* in Tsavo East National Park, Kenya. *Ibis (Lond. 1859).*, 541–544 (1976).
45. R. E. Moreau, the Breeding Seasons of African Birds. *Int. J. Avian Sci.*, 223–267 (1950).
46. A. R. E. Sinclair, Factors Affecting the Food Supply and Breeding Season of Resident Birds and Movements of Palaearctic Migrants in a Tropical African Savannah. *Ibis (Lond. 1859).*, 480–497 (1978).
47. G. H. Miller, M. L. Fogel, Calibrating $\delta^{18}O$ in *Dromaius novaehollandiae* (emu) eggshell calcite as a paleo-aridity proxy for the Quaternary of Australia. *Geochim. Cosmochim. Acta* **193**, 1–13 (2016).
48. M. T. Hincke, C. P. W. Tsang, M. Courtney, V. Hill, R. Narbaitz, Purification and Immunochemistry of a Soluble Matrix Protein of the Chicken Eggshell (Ovocleidin 17). *Calcif. Tissue Int.* **56**, 578–583 (1995).

**SI Appendix Tables**

**Table S1:** Pearson's R and $R^2$ correlation coefficients and associated p-values in the form of a symmetric matrix. Null hypothesis is that there is no correlation between the variables in the row versus the column.

| Pearson's R<br>[$R^2$]<br>(p-value) | $\delta^{13}C$ | $\delta^{15}N$ | $\delta^{18}O$ |
|---|---|---|---|
| $\delta^{13}C$ | 1 | -0.28434<br>[0.0809]<br>(0.07537) | 0.51672<br>[0.2670]<br>(p <<0.001) |
| $\delta^{15}N$ | -0.28434<br>[0.0809]<br>(0.07537) | 1 | -0.16678<br>[0.0278]<br>(0.3037) |
| $\delta^{18}O$ | 0.51672<br>[0.2670]<br>(p <<0.001) | -0.16678<br>[0.0278]<br>(0.3037) | 1 |

**Table S2:** Pairs of carbonate $\delta^{13}C$ and $\delta^{18}O$ values from U-series-dated sub-samples. Samples ending in "O" correspond to the outer tablet and "I" correspond to the inner tablet. External errors (1σ) on $\delta^{13}C$ and $\delta^{18}O$ values are 0.179‰ and 0.149‰, respectively. Table of isotope values for all carbonate and organic fractions analyzed at YFT1 can be found in SI Dataset S1D.

| Layer | Sample ID | **$\delta^{13}C$** (‰ VPDB) | **$\delta^{18}O$** (‰ VSMOW) |
|---|---|---|---|
| 1 | YFT-1A-O | -9.27 | 35.46 |
| 1 | YFT-1A-I | -10.34 | 35.25 |
| 1 | YFT-1C-O | -9.98 | 34.29 |
| 1 | YFT-1C-I | -11.08 | 33.43 |
| 1 | YFT-1D-O | -9.82 | 33.77 |
| 1 | YFT-1D-I | -10.53 | 33.94 |
| 1 | YFT-1E-O | -10.45 | 27.85 |
| 1 | YFT-1E-I | -10.93 | 29.08 |
| 3 | YFT-3C-O | -12.35 | 27.79 |
| 3 | YFT-3C-I | -13.40 | 28.57 |
| 6 | YFT-6D-O | -10.99 | 27.43 |
| 6 | YFT-6D-I | -11.90 | 27.53 |
| 6 | YFT-6E-O | -11.17 | 28.83 |
| 6 | YFT-6E-I | -12.19 | 28.22 |
| 10 | YFT-10A-O | -10.02 | 31.08 |
| 10 | YFT-10A-I | -10.81 | 30.76 |
| 10 | YFT-10E-O | -9.01 | 35.27 |
| 10 | YFT-10E-I | -10.42 | 34.69 |
| 12 | YFT-12F-O | -9.71 | 32.86 |
| 12 | YFT-12F-I | -11.65 | 31.51 |
| 12 | YFT-12G-O | -9.20 | 35.28 |
| 12 | YFT-12G-I | -10.54 | 34.75 |
| 12 | YFT-12I-O | -10.80 | 30.90 |
| 12 | YFT-12I-I | -10.67 | 32.09 |
| 12 | YFT-12J-O | -15.28 | 30.29 |
| 12 | YFT-12J-I | -15.89 | 30.69 |
| 12 | YFT-12J-I | -13.14 | 34.31 |
| 12 | YFT-12J-I-2 | -13.90 | 34.20 |

## SI Appendix Figures

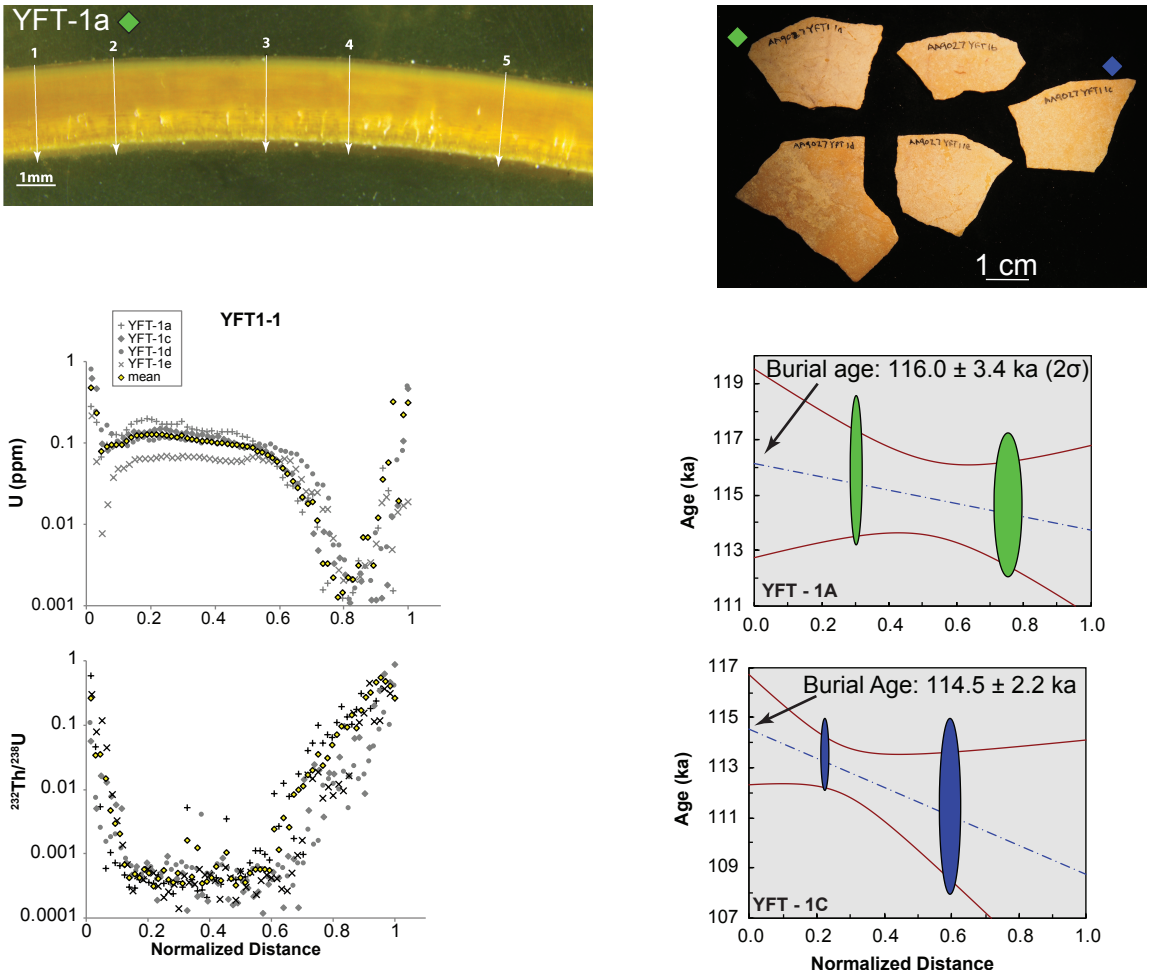


Figure S1: Samples, laser ablation profiles, and $^{230}$Th/U burial age diagrams for samples from Layer Group 1.

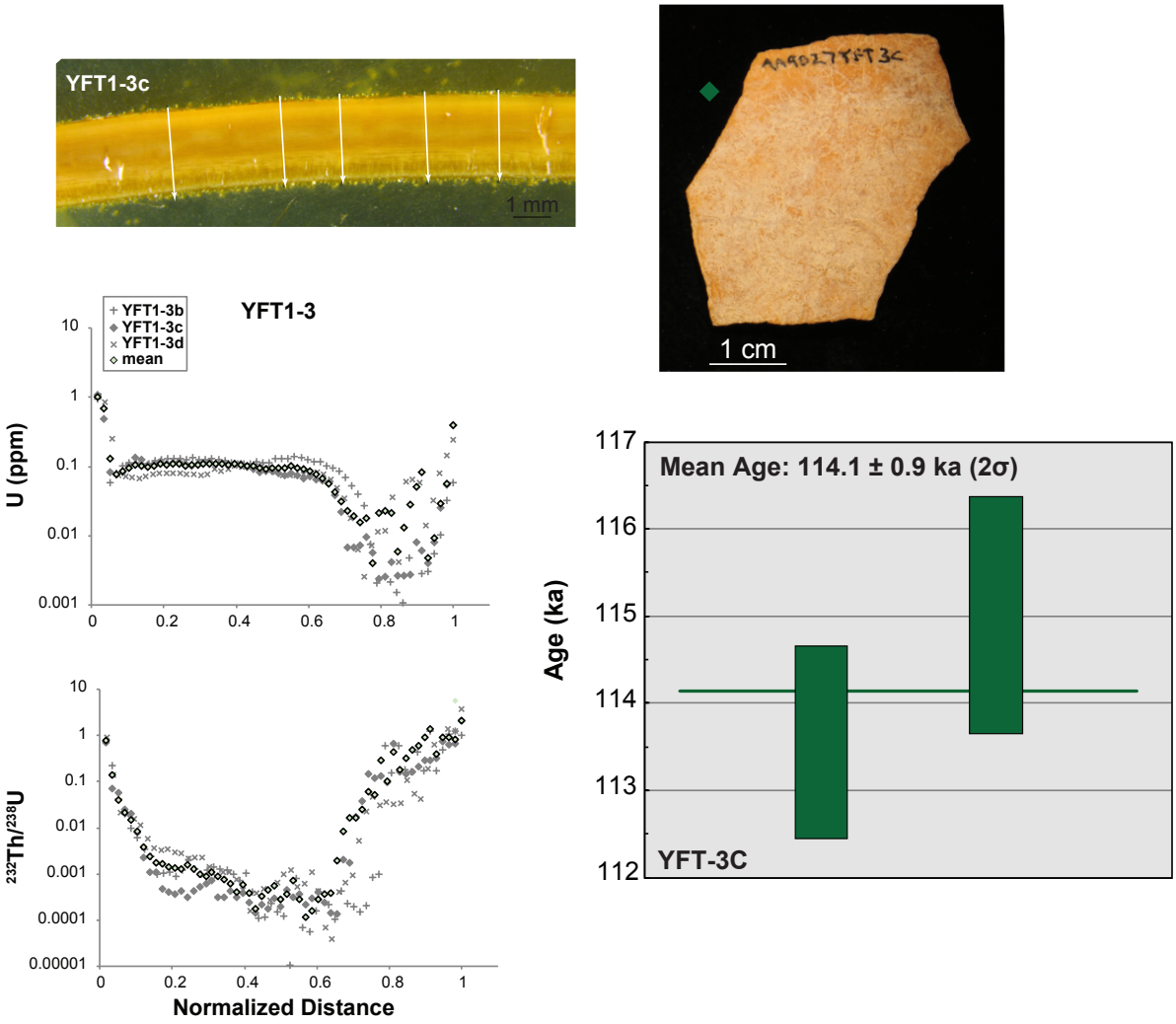


Figure S2: Samples, laser ablation profiles, and $^{230}$Th/U burial age diagrams for samples from Layer Group 3.

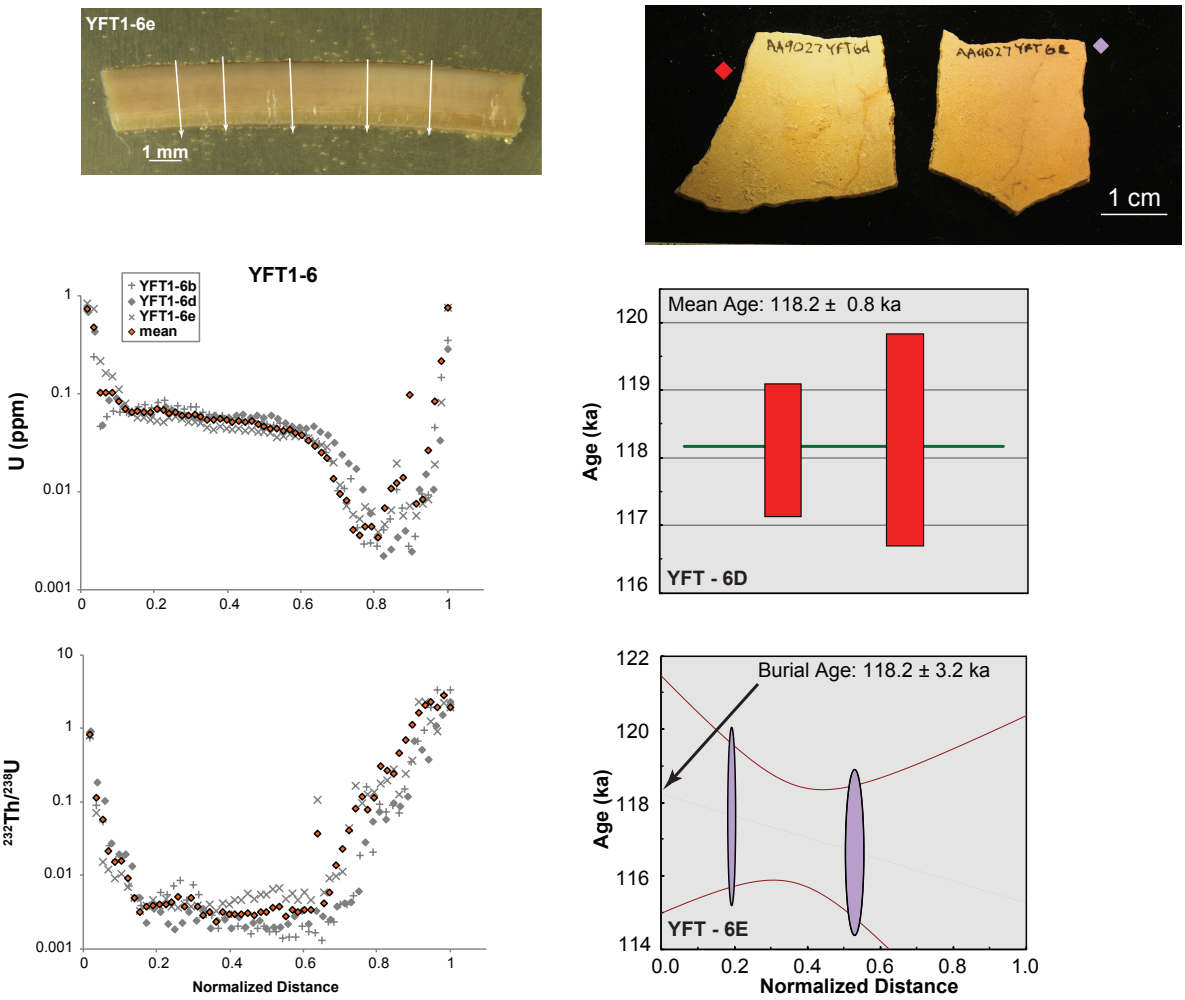


Figure S3: Samples, laser ablation profiles, and $^{230}$Th/U burial age diagrams for samples from Layer Group 6.

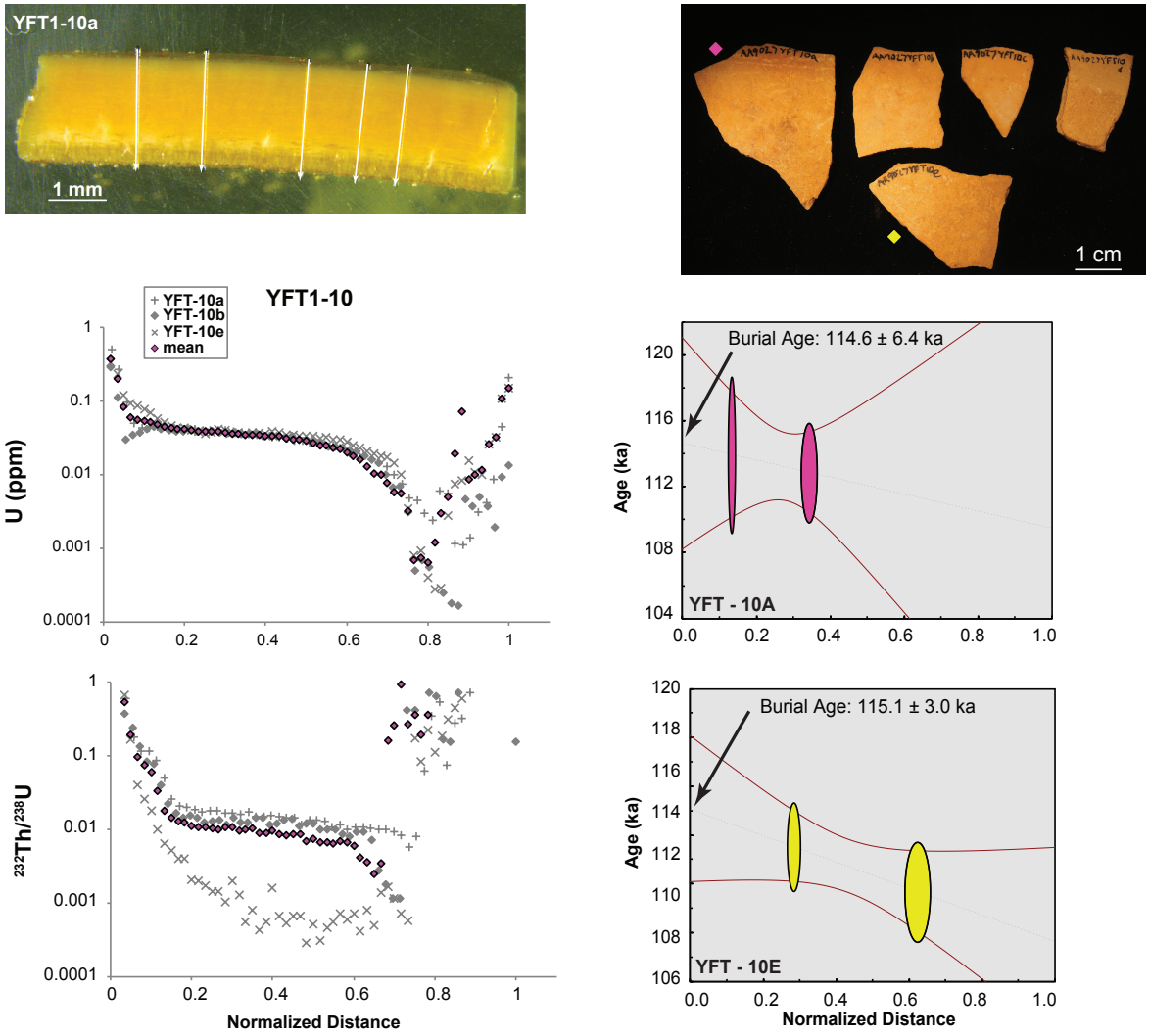


Figure S4: Samples, laser ablation profiles, and $^{230}$Th/U burial age diagrams for samples from Layer Group 10.

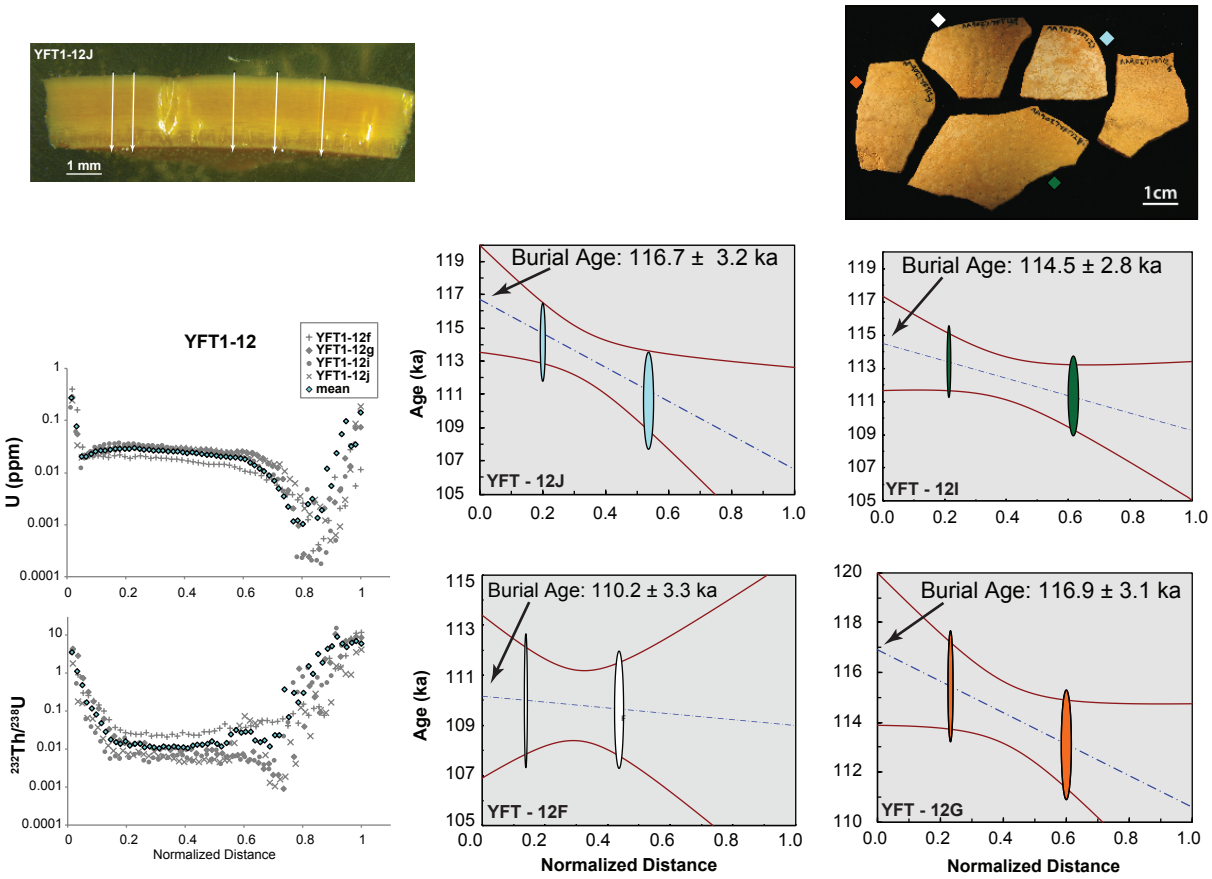


Figure S5: Samples, laser ablation profiles, and $^{230}$Th/U burial age diagrams for samples from Layer Group 12.

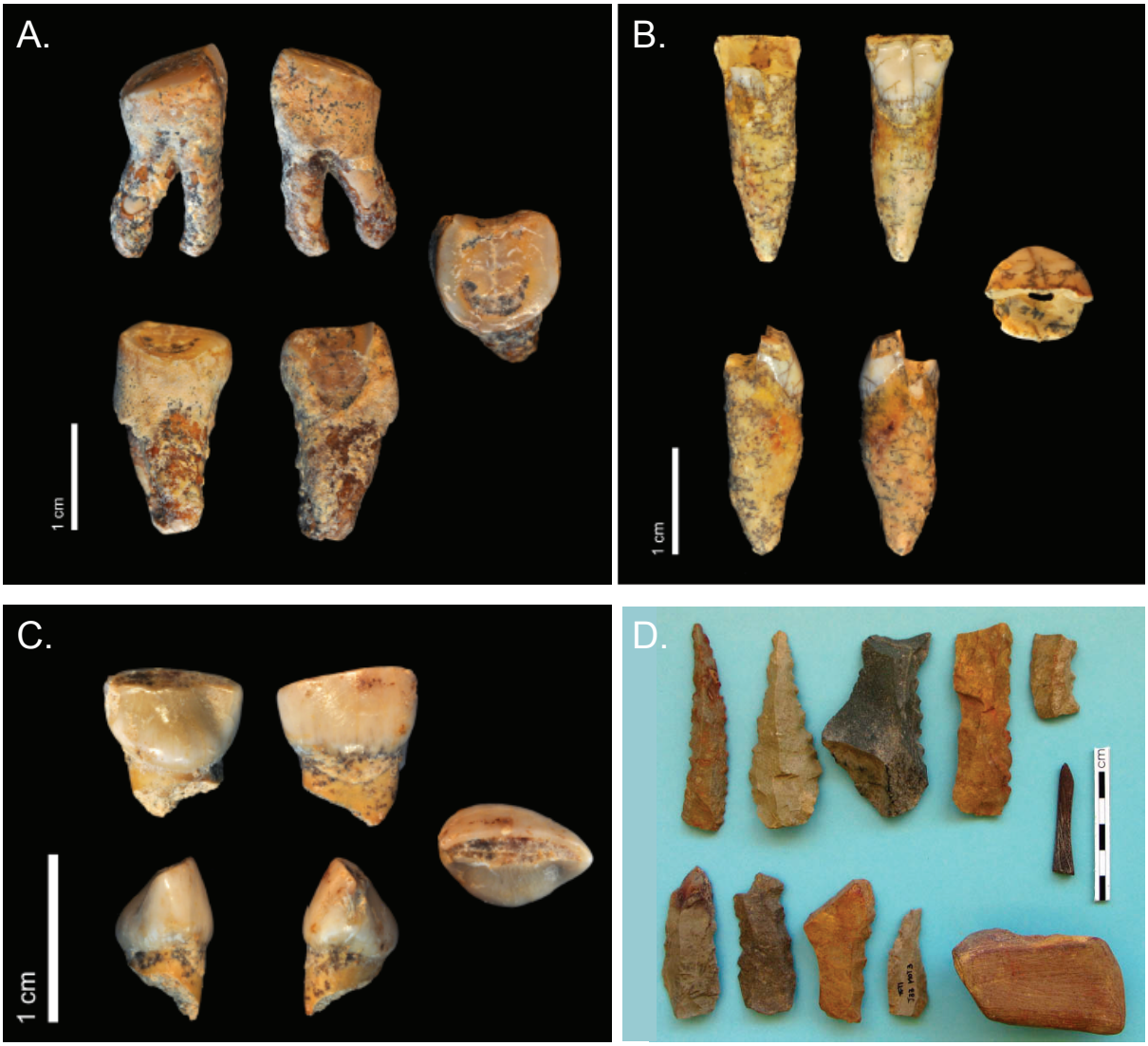


Figure S6: Human teeth and a sample of artifacts recoverd at YFT1. A. Permanent lower right third molar (M3) from layer group 4; B. permanent upper lateral incisor (I2) from layer group 5; deciduous upper central incisor (I1) from layer group 13; D. artifacts, including denticulates, points, red ochre (lower right), all fossil images from Verna et al. (2014) and reprinted with permission from J.-J. Hublin; artifact image c/o R.G. Klein.

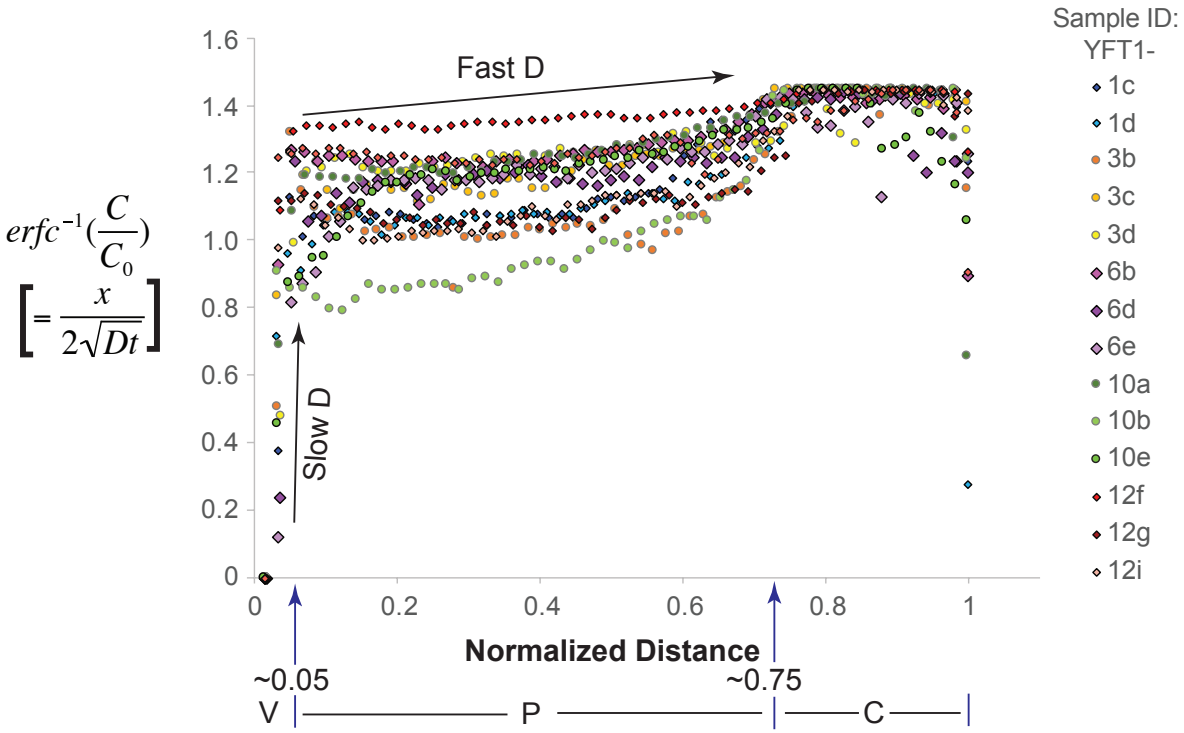


Figure S7: Mean values of laser ablation U concentration profiles plotted as solutions to the 1-dimensional diffusion equation. The slope of points closely tracks changes in crystal structures, denoted by the vertical (V) crystal layer, the palisade (P) layer, and the cone (C) layer calcite crystals in ostrich eggshells. Steeper slope in the vertical crystal layer corresponds with slower diffusion (slow D), while shallower slopes in the palisade layer crystals indicate where faster diffusion occurs (fast D).

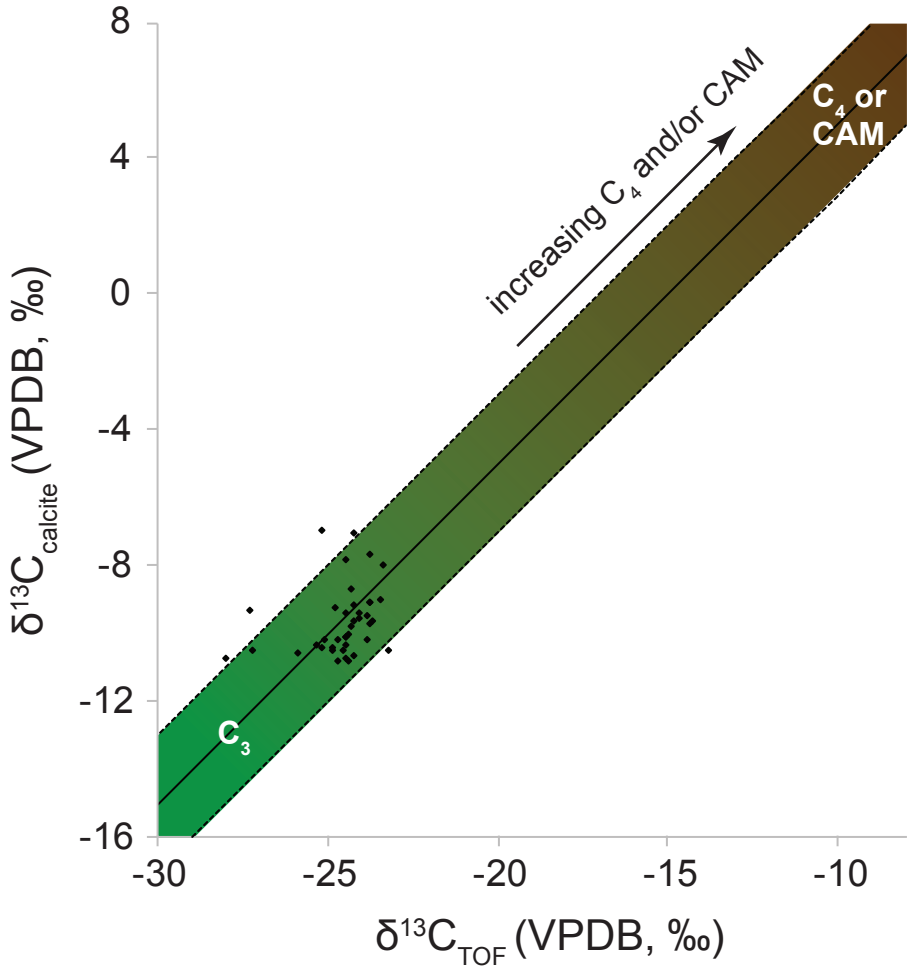


Figure S8: Fractionation between $\delta^{13}C$ of the carbonate (calcite) and total organic fractions (TOF). Samples within the shaded region have a $\Delta^{14}C$ value = 15 ± 2‰, indicating the TOF is unaltered. Samples outside the shaded region have unreliable TOF compositions and so the TOF $\delta^{13}C$ and $\delta^{15}N$ values of these samples are not included in further interpretations. The shaded region also qualitatively indicates the relative amount of $C_3$ vs. $C_4$ or CAM plants in the diet.

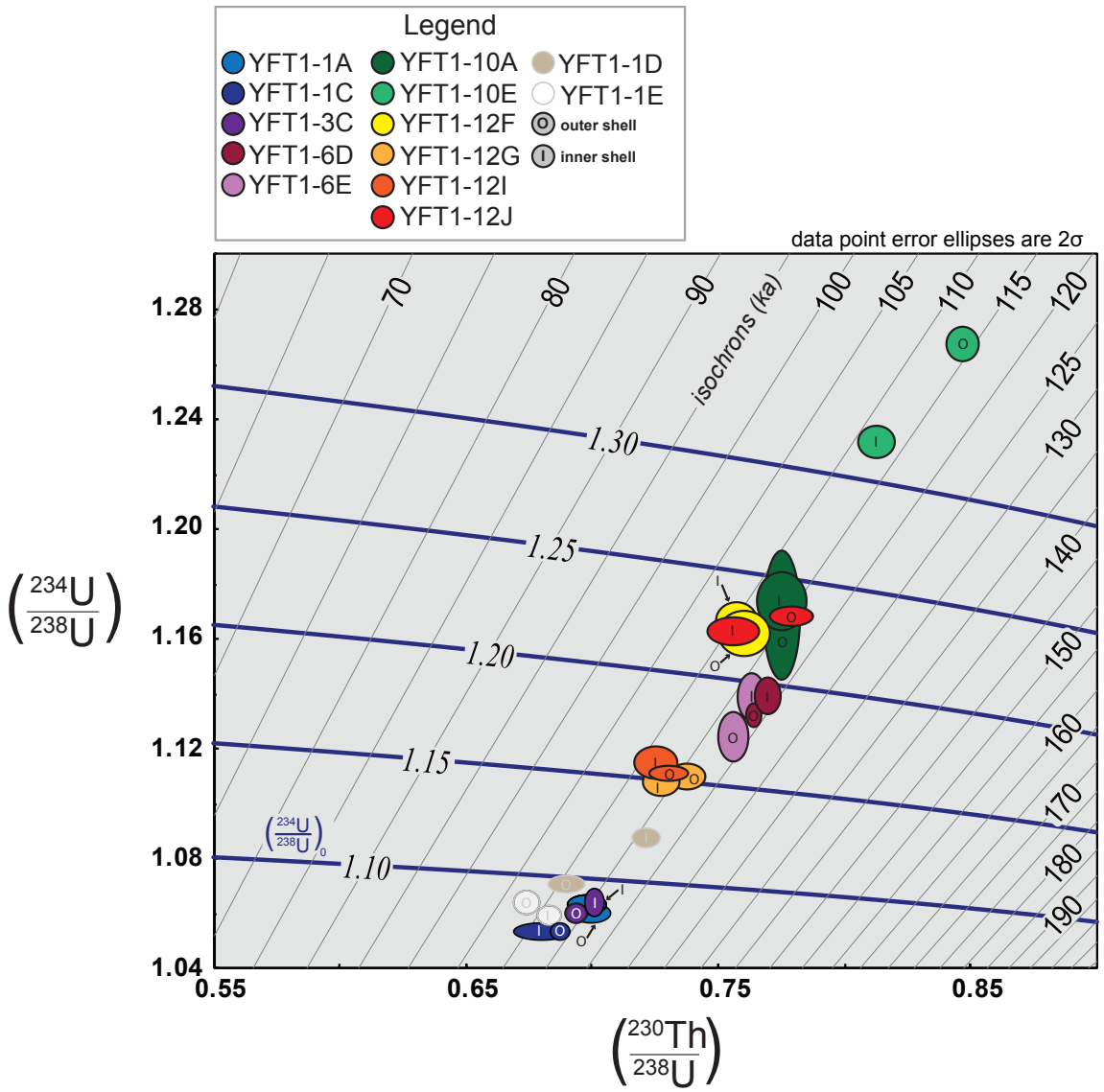


Figure S9: U-series evolution diagram for all dated eggshells. Sub-samples of the same eggshell fragment (denoted by the same color) are plotted of inner and outer shells marked by (I) and (O), respectively. Error ellipses encompass 2σ uncertainty of corrected activity ratios. Burial ages are calculated from samples whose outer shell age > inner shell age; burial ages are not plotted here. Two samples from Layer Group 1 (gray outlines) did not satisfy internal criteria to calculate $^{230}$Th/U burial ages; all other sample (black outlines) were used to calculate burial ages. Blue isopleths are lines of constant $(^{234}U/^{238}U)_0$, showing $(^{234}U/^{238}U)_0$ agrees between most sub-samples, and some samples from the same cluster around similar $(^{234}U/^{238}U)_0$. Gray lines are lines of constant age (isochrons), labeled in thousands of years (ka).

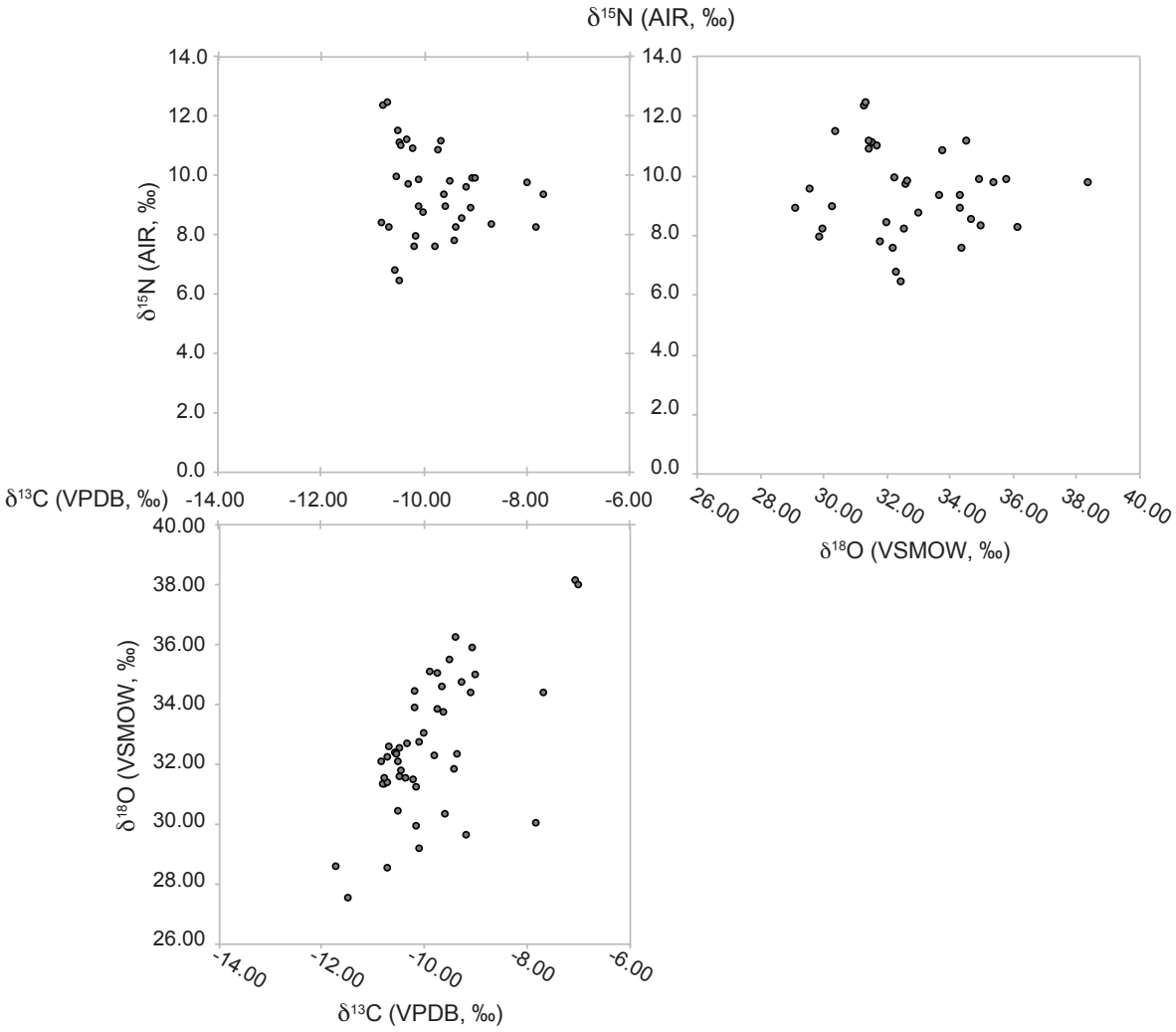


Figure S10: Bi-plots of the three stable isotope systems. There are no significant correlations between any two variables – see Table of correlation values (SM Table 1).

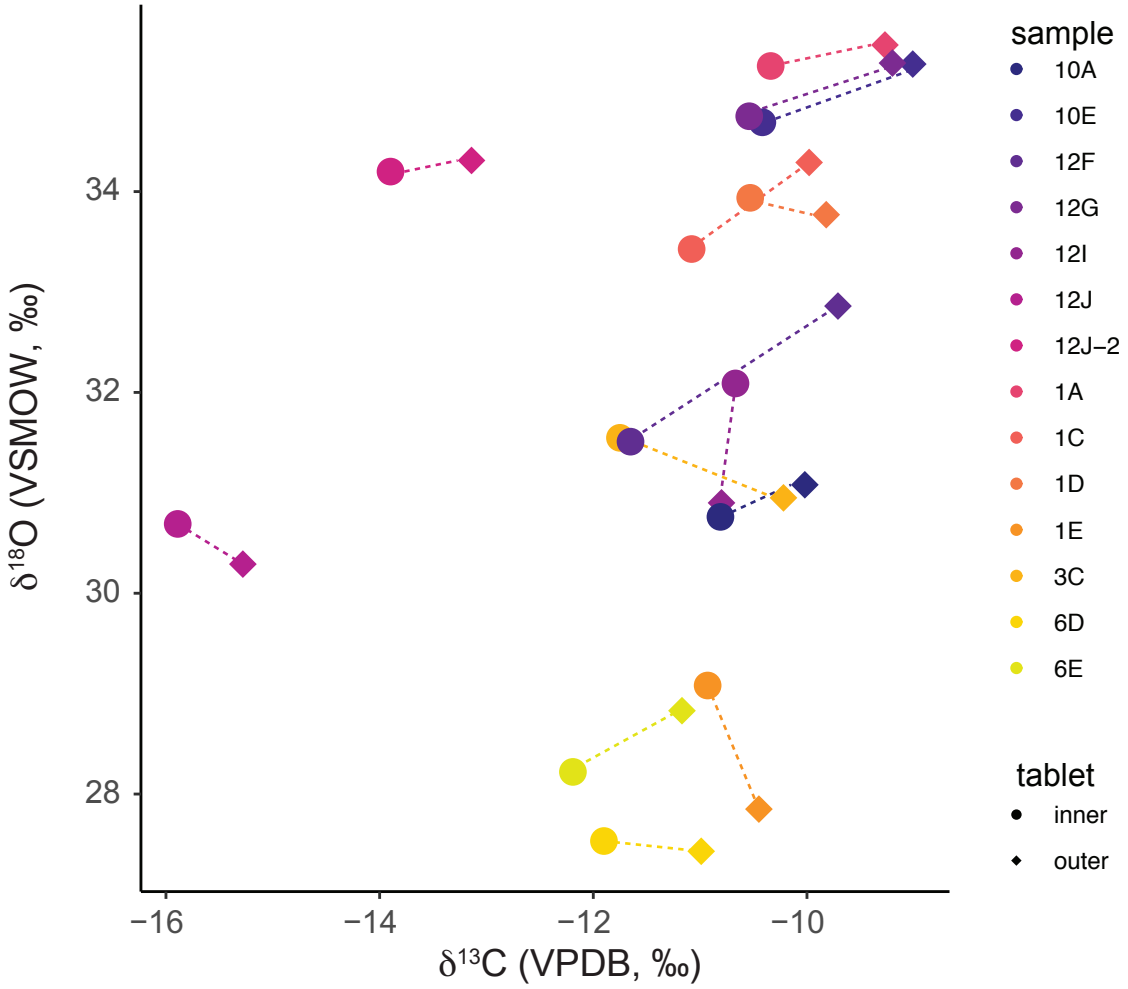


Figure S11: Pairs of inner and outer shell $\delta^{13}C$ and $\delta^{18}O$ values for all dated samples. The outer shell samples consistently have higher $\delta^{13}C$ values, while $\delta^{18}O$ values of the outer shell are mostly higher than the inner shell, but they have greater variability than the pairs of $\delta^{13}C$ values. See Supplementary Results and Discussion for interpretations.